Mineralogical and gemological characterization of emerald crystals from Paraná deposit, NE Brazil: a study of mineral chemistry, absorption and reflectance spectroscopy and thermal analysis

José Ferreira de Araújo Neto[1]* , Sandra de Brito Barreto[1] , Thais Andressa Carrino[1] ,
Axel Müller[2] , Lauro Cézar Montefalco de Lira Santos[1]

Abstract

The Paraná deposit, located at Southwestern Rio Grande do Norte state, in Brazil, is one of the few emerald deposits found at Borborema Province. The mineralization occurs in phlogopite schists and actinolite-phlogopite schists associated with pegmatites and albitites within the Portalegre Shear Zone. Unlike other well-known Brazilian emerald deposits, the mineralogy of Paraná emeralds has remained poorly investigated for the last 40 years. In this study, we conducted mineralogical characterization of theses emeralds through gemological testing, mineral chemistry, absorption and reflectance spectroscopy, and thermal analysis. The Paraná emeralds are bluish-green colored, characterized by high refractive index, several two-phase fluid inclusions and mica is the main mineral inclusion. Electron probe microanalysis and laser ablation-inductively coupled plasma-mass spectrometry analyses detected the presence of Fe^{2+} (0.43–1.94 wt.% FeO) and Cr^{3+} (0.04–0.14 wt.% Cr_2O_3) as the main chromophores replacing octahedral Al^{3+} in the crystal structure. In addition, substantial amounts of MgO (0.40–2.72 wt.%), Na_2O (0.50–1.81 wt.%), and Cs_2O (0.07–0.44 wt.%) were also identified. The main causes for its coloration were attributed to Cr^{3+} absorption features in visible spectral range, which were corroborated by absorption and reflectance spectra. The presence of types I and II H_2O at channel-sites was recorded in Fourier-transform infrared spectra and demonstrated by dehydration processes observed in different thermal and thermogravimetric analyses.

KEYWORDS: Paraná emerald; mineralogy; gemology; geochemistry; spectroscopy.

INTRODUCTION

Emerald is a green gem variety of beryl ($Be_3Al_2Si_6O_{18}$). Its coloration is due to amounts of Cr^{3+}, V^{3+} or Fe replacing Al^{3+} at the Y site in the crystal structure, and it needs a specific geological environment to bring together such chromophore elements, which are commonly concentrated in mafic and ultramafic rocks, whereas Be is originated from Be-bearing pegmatites or, in some cases, brine fluids (Walton 2004).

The beryl structure was firstly reported by Bragg and West (1926) and it consists of an Al or Y site octahedrally coordinated by six oxygen atoms and Be and Si sites both tetrahedrally coordinated by four oxygen atoms. The arrangement of SiO_4 tetrahedra forms stacked six-membered rings, which results in channel sites parallel to the crystallographic c axis.

According to Wood and Nassau (1968), these channels can allow the entrance of alkali ions, such as Na, Cs, Rb and K, as well as two types of water molecules: type I H_2O, with no association to alkali ions, and type II H_2O, coordinated with alkali ions. Type II H_2O can be singly (H_2O IIs) or doubly coordinated to an alkali ion (H_2O IId). The latter occurs in highly hydrated systems with two water molecules surrounding an alkali ion.

At the Borborema Province, Northeastern Brazil, emerald mineralizations are particularly uncommon. Punctual well known deposits are Tauá (Ceará state), which is recognized by low-quality emerald crystals (Schwarz 1987), and the recently discovered Fazenda Bonfim occurrence (Cavalcanti Neto and Barbosa 2007), within the Seridó Mobile Belt (Rio Grande do Norte state), which presents gem-quality crystals that were targeted for prospective activities and scientific research in the last decade (*i.e.*, Scholz *et al.* 2010, Zwaan *et al.* 2012, Santiago *et al.* 2018).

The Paraná emerald deposit is located at the extreme Southwest of Rio Grande do Norte state and has been known since the 1980s. It has been recognized by considerable amounts of gem-quality crystals found in quartz and pegmatite veins hosted in biotite/phlogopite schists (Vasconcelos 1984, Moraes 1999). During such period, emeralds crystals were explored by local miners until almost exhaustion. Brief descriptions of the

[1]Departamento de Geologia, Universidade Federal de Pernambuco – Recife (PE), Brazil. E-mails: araujoneto.geo@gmail.com; sandradebritobarreto@gmail.com; thais.carrino@gmail.com; lauromontefalco@gmail.com

[2]Natural History Museum – Oslo, Norway and Natural History Museum – London, United Kingdom. E-mail: a.b.muller@nhm.uio.no

*Corresponding author.

geological framework at the Paraná region were performed by the Geological Survey of Brazil in regional geological mapping (Medeiros 2008, Souza 2017), but the emerald mineralogical characterization remains uninvestigated. Recent mining activities in the region have been retaken by Mineração Limeira Comércio, Exportação e Importação Ltda, by opening a new commercial possibility for emerald from the Paraná deposit.

Since the Paraná emerald deposit is poorly known and may present important clues on the gemological-geological aspects of Borborema Province, this paper combines several analytical techniques, such as gemological study, mineral chemistry, absorption and reflectance spectroscopy, as well as thermal analysis to introduce and compose the mineralogical characterization of Paraná emerald crystals. Our aim is to investigate internal features and gemological properties, as well as the spectral signature and chemical composition of Paraná emerald, identifying chromophore elements responsible for the green coloration and the main substitutions at the Y and channel sites, generating suitable data that allow comparison with other emerald crystals found worldwide.
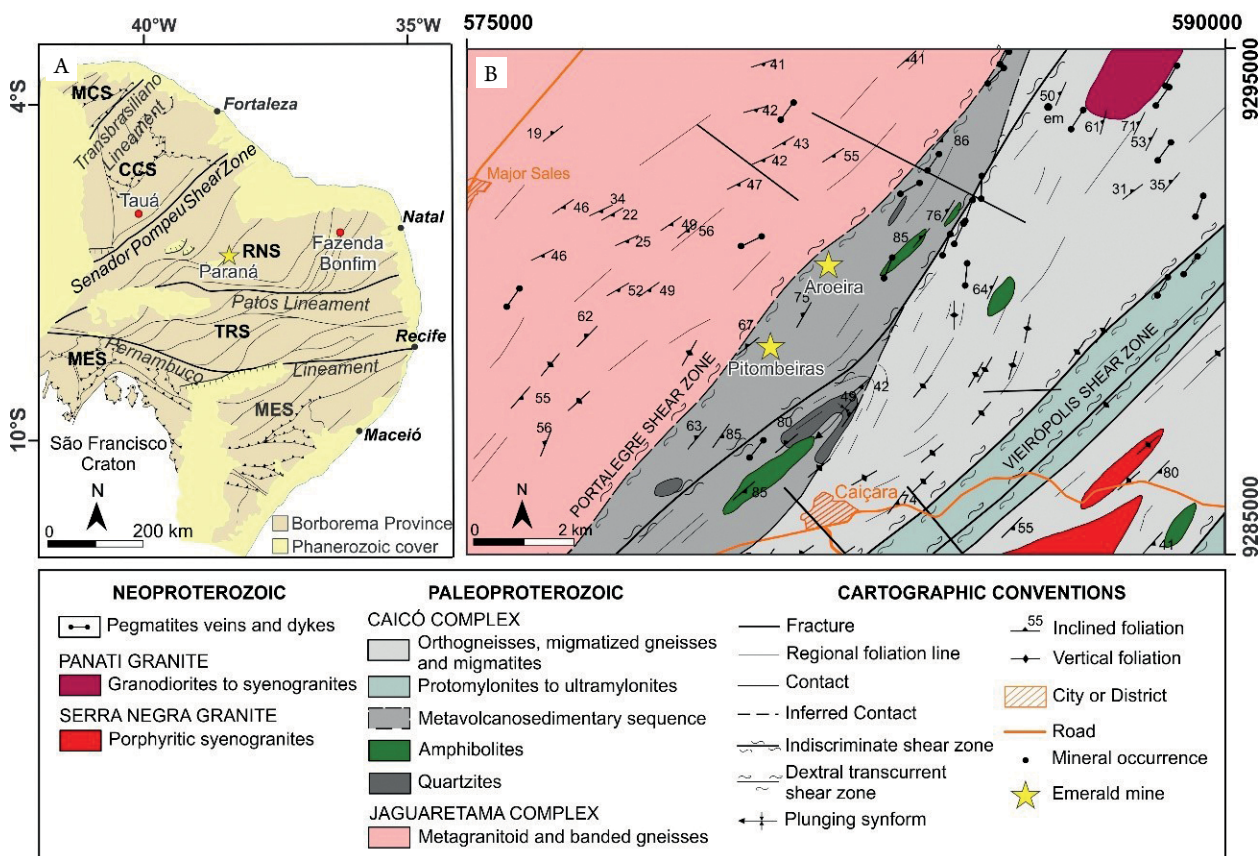
GEOLOGICAL SETTING

Paraná deposit is situated in the Rio Grande do Norte Sub-province of the Borborema Province (Fig. 1A). This sub-province is characterized by several major ductile shear zones that are probable Ediacaran-Cambrian in age (Brito Neves et al. 2000, Medeiros 2008, Viegas et al. 2014). Emerald mineralization occurs along the transcurrent Portalegre Shear Zone, in a discontinuous NE-SW trend with, at least, 20 km length (Moraes 1999). This regional-scale structure represents the contact between meta-granitoids of Jaguaretama Complex and both meta-plutonic and metavolcanossedimentary units of Caicó Complex (Medeiros 2008). The Paraná region is characterized by occurrences of phlogopite and actinolite-phlogopite schists that are part of the metavolcanossedimentary sequence of Caicó Complex (Fig. 1B), which also comprises spatially associated mylonites, gneisses, amphibolite, and quartzites.

The phlogopite and actinolite-phlogopite schists occur as vertical to subvertical lenses along mylonitic domains of Portalegre Shear Zone (Fig. 2A). They host several recrystallized veins and veinlets with granitic composition and aplitic to pegmatitic texture. These granitic bodies occur as *boudins* constituted mostly by quartz and/or feldspar and minor biotite (Fig. 2B). The emerald crystals have grown into the schists, as well as in these small granitic bodies or at the contact between both rocks (Fig. 2C).

Several granitic pegmatites have been reported within the Portalegre and Vieirópolis shear zones (Araújo Neto et al. 2018). At the Paraná deposit, centimeter- to meter-sized granitic pegmatite lenses and veins are found in association with the emerald host rocks. These pegmatites often present a simple

MCS: Médio Coreaú Sub-province; CCS: Ceará Central Sub-province; RNS: Rio Grande do Norte Sub-province; TRS: Transversal Sub-province; MES: Meridional Sub-province.

Figure 1. Regional geological setting of Paraná emerald deposit. (A) Main emerald deposits within the tectonic subdivisions of Borborema Province. Modified from Santos *et al.* (2014). (B) Geologic map of Paraná region with the localization of Aroeira and Pitombeiras mines. WGS 84 horizontal projected datum UTM zone 24S. Modified from Araújo Neto et al. (2018).

composition that is made up of potassium feldspar with minor quartz and muscovite.

At least two main mines are recognized at the Paraná deposit: the Pitombeiras and the Aroeira mines. In these mine shafts, meter-sized dykes of sodium-rich plagioclase (albitite) can be found adjacent to the basement gneisses and host schists. These albitites occur as tabular sheared pegmatite bodies (Fig. 2D), which are mostly composed by albite but with minor light green muscovite.

SAMPLING AND ANALYTICAL METHODS

Emerald samples were collected in Pitombeiras and Aroeira mines or provided by Mineração Limeira Comércio Exportação e Importação Ltda. We examined three faceted emerald gemstones ranging from 0.98 to 3.55 ct, three polished parallel plates, three samples of pulverized emerald, and 20 thin sections made from emerald crystals and emerald-bearing rocks.

Standard gemological study was carried out at the Gemology Laboratory of Universidade Federal de Pernambuco (LABGEM – UFPE). A Schneider RF2 refractometer with polarizing filter and a refractive index fluid (n = 1.79) were employed to measure the refractive index and birefringence. Weight and specific gravity were obtained by a Shimadzu AUY220 hydrostatic digital analytical balance, with a sensibility of 0.1 mg.

Internal features were observed through transmitted light (TL), polarized light (PL), and dark field illumination (DFI) using a Schneider gemological microscope coupled with the Zeiss-Stemi (Stemi 2000-C) optical system and a Schneider horizontal oil-immersed gem microscope also coupled with the Zeiss-Stemi (Stemi 2000-C) optical system, both with maximum magnification of 50x. A calcite dichroscope was used for pleochroism observation. The Chelsea filter was employed for color variation test and short- and long-wave ultraviolet (UV) lamps were used to observe fluorescence.

Major and minor element chemical analysis was carried out on 15 emerald crystals (99 spots) in eight thin sections at the Electron Microprobe Laboratory of the Universidade de Brasília (LASON – UnB). The thin sections were previously carbon-coated in an Edwards Auto 306 vacuum chamber. Chemical data were obtained by JEOL JXA-8230 electron microprobe, equipped with a scanning electron microscope (SEM), five wavelength dispersive X-ray spectrometers (WDS), and one energy dispersive X-ray spectrometer (EDS). The system was operated for standard silicate analysis, using LASON's internal standards for multi-standard calibration: albite (Na), forsterite (Mg), topaz (F), microcline (Al, Si and K), andradite (Ca and Fe), vanadinite (Cl and V), $MnTiO_3$ (Ti and Mn), Cr_2O_3 (Cr), NiO (Ni), and pollucite (Cs). The following parameters were used: acceleration voltage of 15 kV, with bean current of 10 nA, bean diameter of 1 μm, and a 10-second
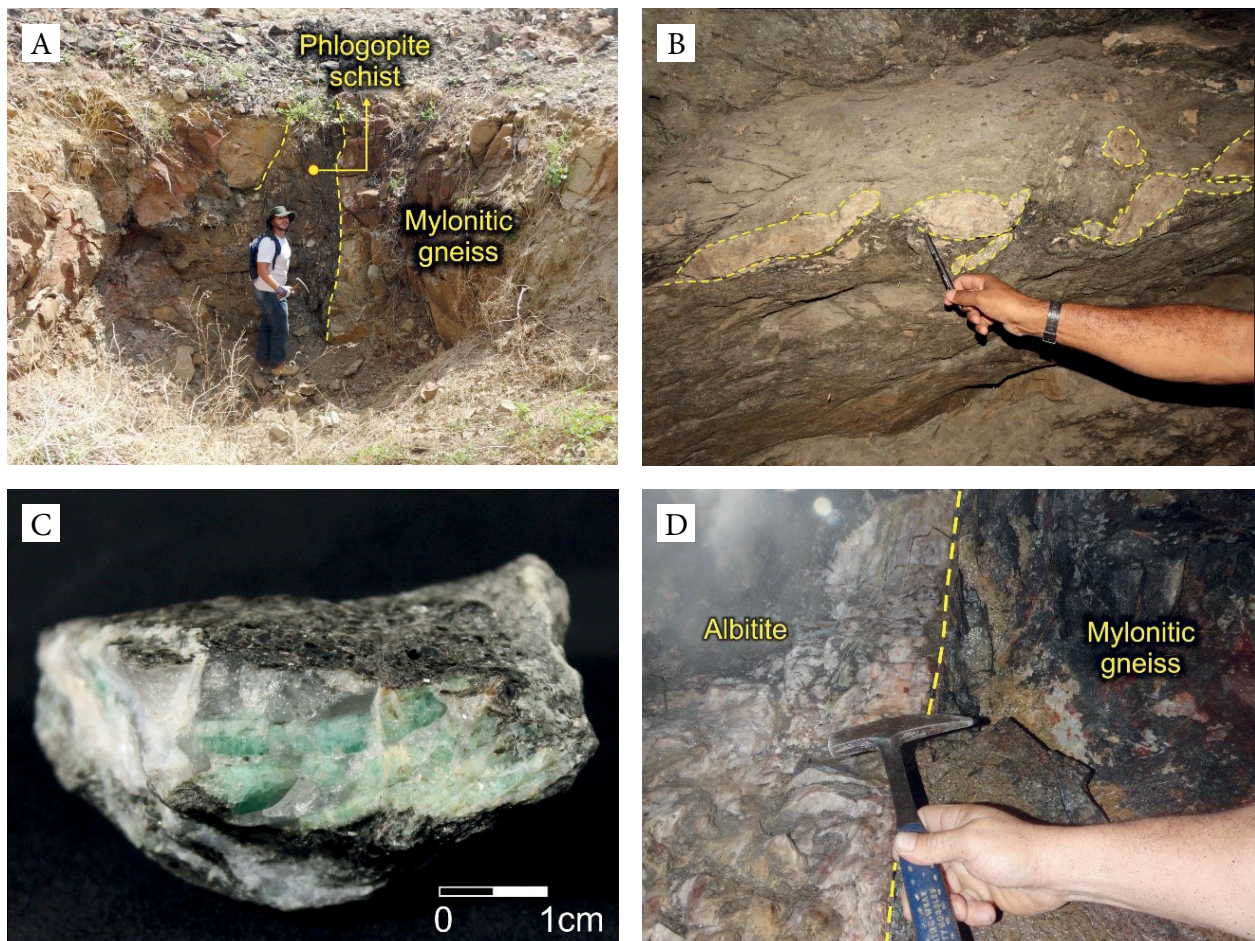
Figure 2. Geological features of Paraná emerald deposit. (A) Vertical contacts between phlogopite schist and mylonitic gneiss. (B) Quartz-feldspar *boudins* inserted in the phlogopite schist on a gallery wall at Pitombeiras mine. (C) Light-colored emerald prisms in a quartz vein hosted in the phlogopite schist. (D) Contact between albite pegmatite (albitite) and mylonitic gneiss at Pitombeiras mining front.

count time for peak. Optical microscope images from CCD video camera and backscattered electron images were used for selecting analysis spots and avoiding mineral inclusions.

Minor and trace elements were determined by laser ablation-inductively coupled plasma-mass spectrometry (LA-ICP-MS) conducted in 12 thin sections of emerald crystals. The analysis was performed at the Geological Survey of Norway, using a double-focusing sector field mass spectrometer, model ELEMENT XR, from Thermo Scientific, which is combined with a NewWave UP193FX laser probe. The 193-nm laser had a repetition rate of 20 Hz, a spot size of 75 μm, and an energy fluence of 5.5 to 6.5 mJ/cm^2 on the sample surface. A continuous raster ablation with laser speed of 15 μm/s on an area of approximately 300 × 150 μm was applied in the emerald crystals. The isotope ^{29}Si was used as internal standard, by applying Si concentration obtained through electron microprobe or stoichiometric concentration of Si in $Be_3Al_2SiO_6$ for emerald crystals without microprobe chemical data. External multi-standard calibration was performed using the reference materials NIST SRM 610, 612, and 614 and 1830, BAM No.1 amorphous SiO_2 glass from the Federal Institute for Material Research and Testing in Germany, the Qz-Tu synthetic pure quartz monocrystal provided by Andreas Kronz from the Geowissenschaftliches Zentrum Göttingen (GZG), Germany. Certified, recommended, and proposed values for these reference materials were taken from Jochum *et al.* (2011) and from the analysis certificates, where available. Each measurement comprised 15 scans of each isotope. An Ar blank was run before each reference material and sample measurement to determine the background signal. The background was subtracted from the instrumental response of the reference material/sample before normalization against the internal standard, in order to avoid instrumental drift effects. This was carried out to avoid memory effects between samples. A weighted least squares regression model, including several measurements of the six reference materials, was used to define the calibration curve for each element.

Visible-near infrared absorption spectra were obtained for three double-sided polished emerald plates using a PerkinElmer spectrophotometer, Lambda 35 model, at the Ionizing Radiation Metrology Laboratory of Universidade Federal de Pernambuco. The spectrophotometer operated in the 400–1,100 nm spectral range, with 4 nm slit, data interval of 1 nm and scanning speed of 120 nm/min. Short-wave and mid-wave infrared spectra of the same three samples were obtained at the Mineral Technology Laboratory of Universidade Federal de Pernambuco, using a Bruker Fourier-transform infrared (FT-IR) spectrometer, model Vertex 70, operating in a range from 7,500 to 1,500 cm^{-1} with an 128x scanning and a resolution of 4 cm^{-1}.

Reflectance spectroscopy was conducted in 10 rough and faceted emerald crystals, using FieldSpec4™ Standard Resolution spectroradiometer (Analytical Spectral Devices) at the Institute of Geoscience of the Universidade Estadual de Campinas (UNICAMP). The spectroradiometer records spectra in 2,151 channels, with wavelengths ranging from 350 to 2,500 nm that comprise the visible to near infrared range (VNIR, 350–1,200 nm) and the short-wave infrared range (SWIR, 1,200–2,500 nm). The spectral resolution is 1.4 nm for the 350–1,000 nm range, and 1.1 nm for 1,001–2,500 nm (Malvern Panalytical 2018). A contact probe with internal light source and ~20 mm spot size was used. Data were calibrated using a Spectralon® white plate. The samples were measured at least three times, and an average reflectance curve was calculated for each sample.

Differential thermal and thermal gravimetric analyses were performed simultaneously in three emerald powder samples at the Mineral Technology Laboratory of Universidade Federal de Pernambuco, using a Shimadzu thermal analyzer, DTG 60H model, with a heating rate of 10ºC/min and maximum temperature of 1,150ºC. The atmosphere used for the analyses was nitrogen (N_2). Calcined alumina was used as a reference material and an alumina cylindrical crucible was used at 0.5 mm diameter and 0.25 mm height.

GEMOLOGICAL PROPERTIES

Emerald crystals are translucid to transparent and occur as hexagonal prisms with irregular basal termination (Fig. 3A). They show green to bluish green colors, varying from weak to strong saturations (Fig. 3B). Crystals with strong color saturation present expressive greenish blue to yellowish green dichroism under the dichroscope and polarized light microscope (Fig. 3C). Growth and color zoning concentric to the c axis is evidenced in emerald plates parallel to the basal plane (Fig. 3D).

Refractive indexes measurements of the ordinary (n_o = 1.590) and extraordinary (n_e = 1.580–1.583) rays yield a birefringence from 0.007 to 0.010. Average specific gravity is 2.74, and the examined crystals are inert to short- and long-wave UV radiation, besides they do not show a reaction under the Chelsea filter.

The dominant group of inclusions is the two-phase liquid-gas type fluid inclusions (Fig. 4A). Several inclusions exhibit a preferential orientation that corresponds to a crystallographic direction of the emerald crystal (possibly the c axis), thus being considered primary inclusions contemporaneous with the crystal growth. The cavities containing fluid inclusions are parallel to fine growth tubes and have an irregular or rectangular shape. They usually occur as elongated rectangles with straight or cuneiform termination or as negative crystals (crystal-like cavities). Two-phase inclusions were also observed in partially healed fissures (Fig. 4B). These inclusions are considered pseudo-secondary because they are hosted in late-formed fissures, but still during crystal growth. The entangling of numerous fractures cracks and healing fissures confers a *Jardin* aspect to these emeralds (Fig. 4C), due to the resemblance of shrubs in a garden.

Few mineral solid inclusions were encountered. Brownish and greenish mica plates with hexagonal sub-idiomorphic to idiomorphic forms are the main mineral inclusions. These mica crystals occur parallel to the orientation of growth tubes; therefore, they are considered syngenetic solid inclusions (Fig. 4D).

Color-zoned emerald crystals, consisting of hexagonal, concentric growth zones vary from different shades of
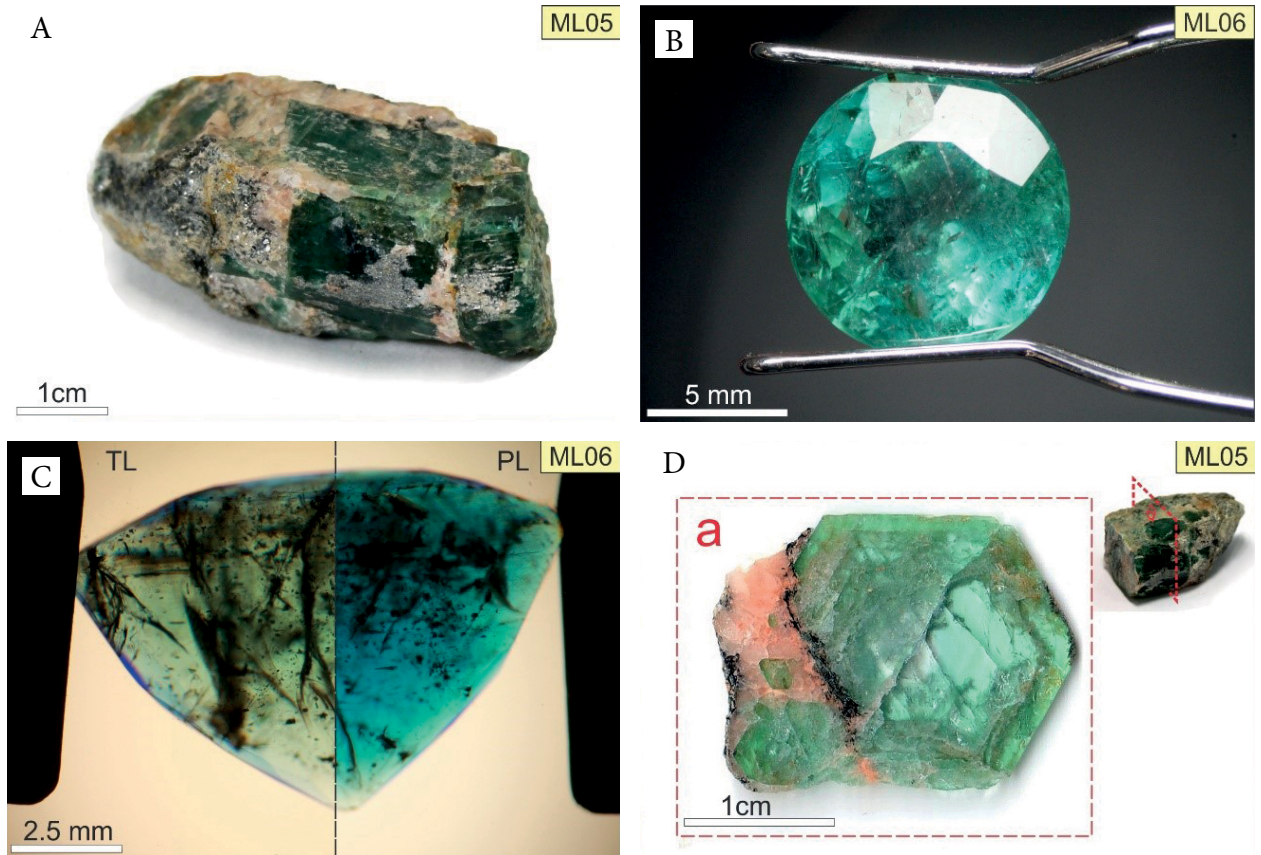
Figure 3. Emerald from Paraná deposit. (A) Rough emerald prism in quartz-feldspar matrix from Pitombeiras Mine. (B) Faceted bluish-green emerald from Aroeira Mine. (C) Dichroism in faceted emerald under transmitted light (TL) and polarized light (PL) in immersion horizontal microscope. (D) Emerald basal section with concentric color zoning and associated feldspar and phlogopite along fractures.
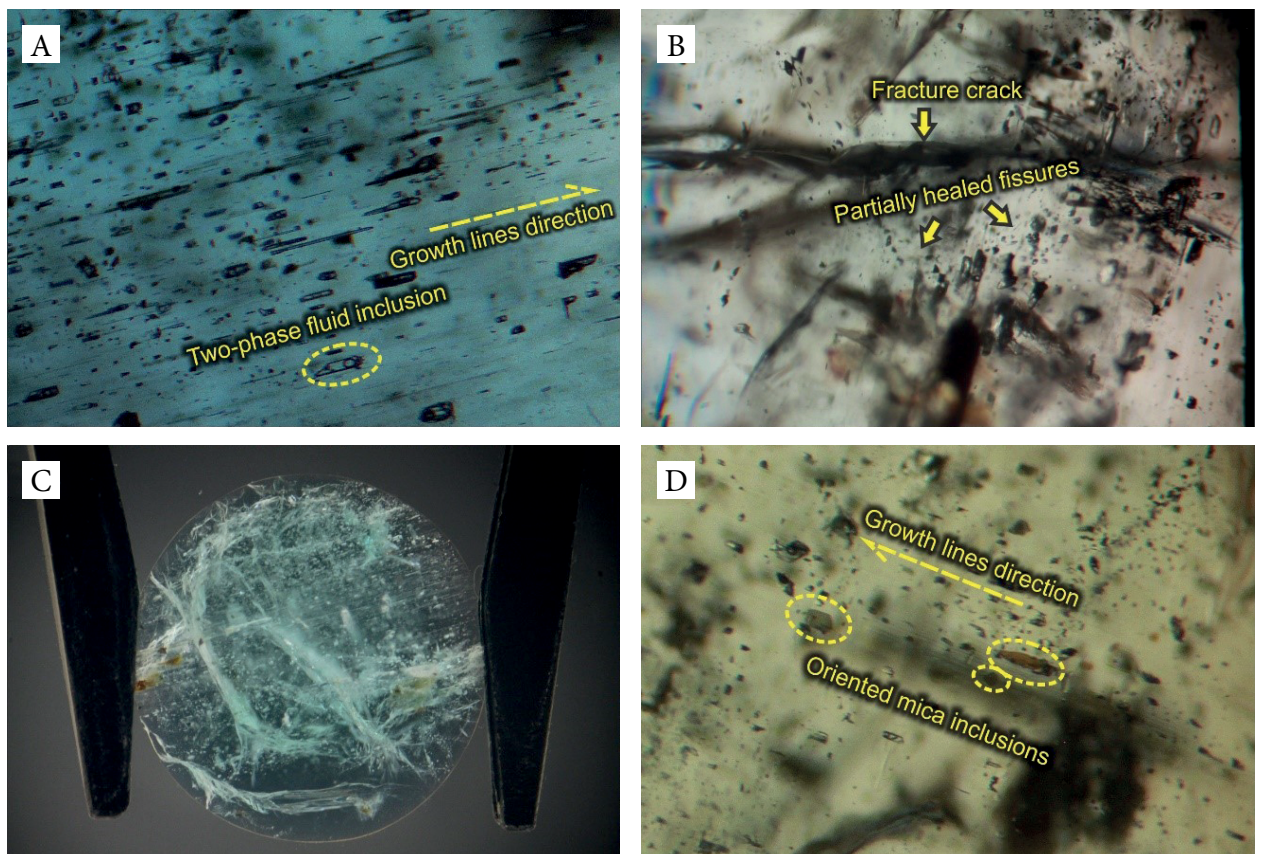
Figure 4. Interior features of a representative Paraná emerald crystal (ML06). (A) Two-phase fluid inclusions parallel to growth lines direction (50x PL). (B) Fluid inclusions in partially healed fissures (50x TL). (C) *Jardin* pattern generated by several fluid inclusions, cracks, and fissures (12.5x DFI). (D) Mica lamellae inclusions parallel to growth lines direction (50x PL).

green to almost colorless. The crystals have two-phase fluid inclusions arranged along the color striations and concentrated in an intermediate zone, immediately external to the central colorless core (Fig. 5A). The distinct boundary between the colorless core and oscillatory zoned green overgrowth indicates a change in the crystallization environment. The oscillatory overgrowth may reflect extrinsic changes of the crystallization environment (P-T, tectonics?) or intrinsic diffusion-controlled growth, whereby the coloring agents become depleted due to fast crystal growth rate or enriched during slow growth.

Zones with high inclusion content were identified with SEM. Qualitative EDS analysis revealed inclusions of quartz, potassium feldspar, and sericitized plagioclase. They delimited two different zones in a hexagonal basal section. The presence of these two zones suggests that the Paraná emeralds have gone through at least two stages of crystal growth (Fig. 5B).

CHEMICAL COMPOSITION

Representative emerald electron microprobe chemical data are presented in Table 1. Paraná emeralds show moderate concentrations of Fe (average 0.94 wt.% FeO) and relatively low Cr (average 0.08 wt.% Cr_2O_3) and V (average 0.02 wt.% V_2O_3). Intense bluish green samples contain these chromophore elements in concentrations, which are 1.4 to 2.6 times higher than those of crystals with less intense color (*e.g.* ML05 sample). The $FeO/(Cr_2O_3+V_2O_3)$ ratio ranges from 5.0 to 21.6.

Concentrations of Mg are moderate to high (average 1.15 wt.% MgO), ranging from 0.40 to 2.72 wt.%. Sodium and Cs are also present in relevant content of 1.00 wt.% Na_2O and 0.16 wt.% Cs_2O. The H_2O content was calculated through the empirical equation of Marshall *et al.* (2016), which established: $H_2O = 0.5401 \ln Na_2O + 2.1867$, leading to an average content of 2.15 wt.% for the Paraná emeralds.

The Li, B, Mn, Ge, Rb, K, Ca, Sc, Ti, and Ga trace elements were detected by LA-ICP-MS (Tab. 2). Average K concentrations range from 210 to 1,811 ppm, while Li is found in relatively low concentrations of 86 to 381 ppm. Manganese, Ti,

Ga, Ge, and B are present in very low concentrations, averaging lower than 50 ppm. Germanium and B have specifically low concentrations of < 5 ppm.

The calculated values for atoms per formula unit (apfu) in Table 1 show deficiency of Al^{3+} at the octahedral coordinated Y structural site (Al < 2 apfu), with mean values varying from 1.460 to 1.855 apfu. This Al^{3+} deficiency is commonly accompanied by accommodation of Cr, V, Fe, Mn, Mg, Ni, and Ti. Figure 6A shows the relationship between the Al content versus the sum of other Y-site cations, exhibiting a strong negative linear correlation, with a Pearson correlation coefficient (r) equal to -0.989. On the other hand, the substitution of Al^{3+} by bivalent cations (*e.g.*, Fe^{2+}, Mg^{2+}, Mn^{2+}, and Ni^{2+}) at the Y-site is associated with coupled substitutions of monovalent cations (*e.g.*, Na^+, K^+, Cs^+) in structural channels to obtain charge balance. As expected, Paraná emeralds have a strong positive linear correlation between the sum of Y-site bivalent cations versus the sum of monovalent cations of the structural channels, with r equal to 0.982 (Fig. 6B). Samples that plot at the right side of the 1:1 straight line suggest that part of the analyzed Fe in emerald is present as Fe^{3+} (Groat *et al.* 2008).

Chemical zoning

EPMA element profiling was carried out on the ML05 crystal, in order to detect which coloring agents are responsible for the observed zoning. Figure 7 illustrates the chemical variation along the sampling profile.

The colorless core has a lower average Al_2O_3 content than the greenish margin (Fig. 7B), which allows an increased uptake of other Y-site cations. MgO is mainly higher in the core, suggesting that Mg^{2+} plays an important role as Al^{3+}-substituent Y-site cation in the core zone. This is accompanied by the uptake of compensating monovalent cations in the structural channels, which is represented by the increase in Na_2O and K_2O concentrations (Fig. 7D). The FeO content shows an erratic behavior in the crystal core. While V_2O_3 behaves erratically across the entire crystal, the Cr_2O_3 content decreases considerably in this central colorless region (Fig. 7E). Thus, elevated
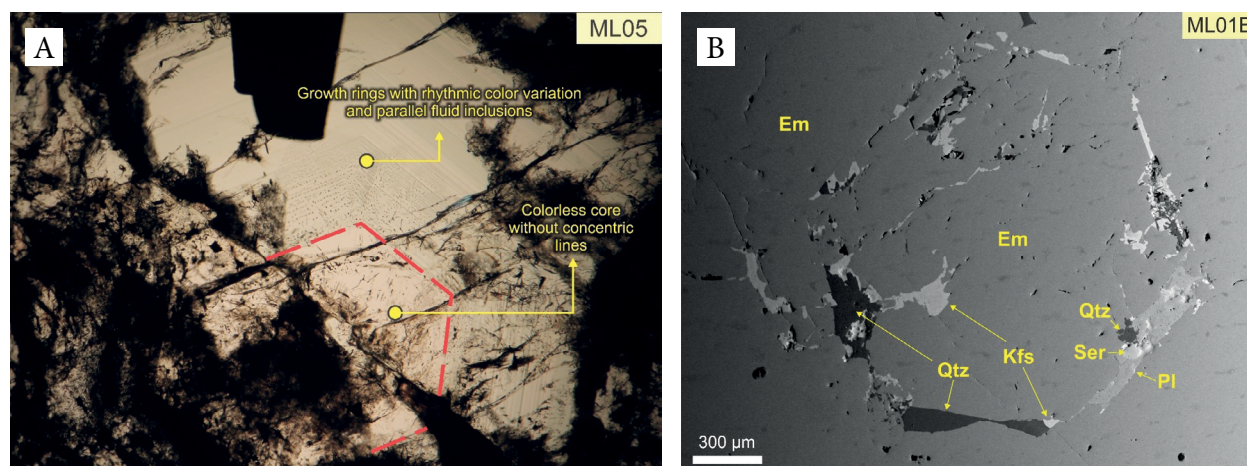
Figure 5. Zoned emerald crystals. (A) Oscillatory concentric color zoning. The red dashed line indicates the boundary between the colorless core and the outer, green growth zones (16x PL). (B) Backscattered electron image shows mineral inclusions of quartz (Qtz), K-feldspar (Kfs), and sercitized (Ser) plagioclase (Pl) delimiting two stages of crystal growth in an emerald crystal (Em).

Table 1. Electron probe microanalysis average chemical composition of Paraná emerald samples.

Sample	EM82 (6)	ML01A1 (3)	ML01A2 (3)	ML01A3 (3)	ML01A4 (3)	ML01A5 (3)	ML01B1 (5)	ML01B2 (4)	ML01B3 (6)	ML04 (15)	ML05 (20)	ML07 (18)	ML08A (3)	ML09A1 (4)	ML09A2 (3)
SiO_2 (wt.%)	65.03	63.91	64.84	64.49	64.57	64.32	65.85	66.05	65.82	65.06	63.28	65.01	63.62	64.93	65.48
TiO_2	0.03	0.00	0.00	0.02	0.01	0.09	0.04	0.02	0.05	0.05	0.07	0.07	0.05	0.03	0.12
Al_2O_3	14.70	15.44	16.10	15.91	15.25	15.36	15.80	15.98	15.36	16.95	13.92	16.55	13.03	16.29	17.10
FeO^*	1.57	0.86	0.73	0.70	0.89	0.91	0.86	0.82	0.97	0.50	1.94	0.70	1.41	0.75	0.43
MnO	0.02	0.01	0.03	0.04	0.03	0.01	0.02	0.03	0.03	0.03	0.02	0.03	0.03	0.01	0.01
MgO	1.50	1.23	0.96	0.84	1.27	1.20	1.26	1.08	1.46	0.43	1.70	0.62	2.72	0.62	0.40
Cr_2O_3	0.06	0.09	0.05	0.06	0.14	0.10	0.12	0.10	0.10	0.08	0.11	0.04	0.06	0.05	0.07
V_2O_3	0.02	0.03	0.02	0.01	0.04	0.02	0.02	0.01	0.01	0.02	0.04	0.02	0.01	0.02	0.00
NiO	0.02	0.00	0.01	0.03	0.02	0.02	0.01	0.02	0.00	0.01	0.02	0.02	0.03	0.02	0.00
CaO	0.01	0.03	0.02	0.02	0.01	0.01	0.02	0.02	0.02	0.01	0.01	0.01	0.09	0.01	0.01
Na_2O	1.35	1.05	0.81	0.73	1.04	1.03	1.11	1.08	1.29	0.51	0.66	0.66	1.81	0.65	0.50
K_2O	0.04	0.03	0.03	0.08	0.06	0.05	0.03	0.04	0.05	0.04	0.13	0.03	0.18	0.03	0.02
Cs_2O	0.12	0.10	0.08	0.07	0.16	0.14	0.12	0.12	0.11	0.16	0.44	0.27	0.24	0.15	0.18
Cl	0.02	0.02	0.00	0.04	0.01	0.01	0.01	0.01	0.01	0.01	0.01	0.00	0.01	0.01	0.00
BeO^{**}	13.41	13.23	13.41	13.31	13.33	13.30	13.62	13.65	13.60	13.48	13.08	13.47	13.13	13.41	13.57
H_2O^+	2.35	2.20	2.07	2.01	2.21	2.19	2.24	2.22	2.32	1.82	2.34	1.96	2.51	1.95	1.81
Total	100.23	98.22	99.15	98.36	99.02	98.76	101.13	101.25	101.20	99.15	98.42	99.46	98.90	98.95	99.71
Si (apfu)	6.055	6.033	6.036	6.049	6.051	6.041	6.037	6.042	6.045	6.027	6.043	6.029	6.051	6.047	6.027
Al	1.612	1.718	1.767	1.760	1.684	1.700	1.707	1.723	1.662	1.850	1.567	1.809	1.460	1.788	1.855
Fe^{2+}	0.122	0.068	0.057	0.055	0.070	0.071	0.066	0.063	0.075	0.038	0.155	0.054	0.112	0.059	0.033
Mn	0.001	0.001	0.002	0.003	0.002	0.001	0.002	0.002	0.002	0.002	0.001	0.002	0.002	0.001	0.001
Mg	0.208	0.173	0.133	0.117	0.177	0.168	0.172	0.147	0.200	0.059	0.242	0.086	0.386	0.086	0.055
Cr	0.004	0.006	0.003	0.004	0.010	0.008	0.009	0.007	0.007	0.006	0.008	0.003	0.004	0.004	0.005
V	0.001	0.002	0.001	0.001	0.003	0.001	0.001	0.001	0.001	0.001	0.002	0.001	0.001	0.001	0.000
Ni	0.002	0.000	0.001	0.002	0.001	0.001	0.001	0.002	0.000	0.001	0.001	0.002	0.002	0.002	0.000
Ti	0.002	0.000	0.000	0.002	0.001	0.006	0.003	0.001	0.003	0.004	0.003	0.005	0.003	0.002	0.008
Y-site (total)	1.952	1.969	1.965	1.943	1.948	1.957	1.960	1.946	1.950	1.962	1.980	1.963	1.971	1.942	1.958
Ca	0.001	0.003	0.002	0.002	0.001	0.001	0.002	0.002	0.002	0.001	0.003	0.001	0.009	0.001	0.001
Na	0.243	0.191	0.145	0.132	0.188	0.187	0.197	0.191	0.230	0.091	0.247	0.118	0.333	0.118	0.089
K	0.005	0.004	0.003	0.010	0.007	0.007	0.004	0.005	0.005	0.004	0.016	0.004	0.021	0.004	0.002
Cs	0.005	0.004	0.003	0.003	0.006	0.006	0.005	0.005	0.004	0.006	0.018	0.011	0.010	0.006	0.007
R (total)	0.254	0.202	0.153	0.147	0.203	0.200	0.208	0.202	0.242	0.102	0.284	0.133	0.373	0.129	0.100
Be	3.000	3.000	3.000	3.000	3.000	3.000	3.000	3.000	3.000	3.000	3.000	3.000	3.000	3.000	3.000

The number of analyzed spots per sample is given in parenthesis. *Total iron presented as FeO; **determined by stoichiometry based on 3 Be and 18 O apfu; †calculated using the equation $H_2O = 0.5401 \ln Na_2O + 2.1867$ (Marshall et al., 2016).

Cr^{3+} concentrations might be responsible for high green color intensities of Paraná emeralds.

SPECTROSCOPY

The absorption spectra of three double polished plates of emerald samples in the visible-near infrared range exhibit a broad absorption band with maximum absorption at 603–608 nm, derived from electronic transitions in Cr^{3+} at the octahedral Y-site (transition $^4A_2 \rightarrow ^4T_2$, Wood and Nassau 1968). Subtle absorption features are present at 425–430, 682–684 and 637 nm. They all indicate the presence of Cr^{3+} in the crystal structure.

A second broad absorption occurs in the range of 829–836 nm and it is attributed to the $^5T_2 \rightarrow ^5E$ transition in Fe^{2+} at the octahedral Y-site (*cf.* Wood and Nassau 1968, Rondeau *et al.* 2008, Zwaan *et al.* 2012). Characteristic absorption VNIR spectra for Paraná emeralds are shown in Figure 8.

Spectra obtained by FT-IR spectroscopy applied on the same three emerald samples are characteristically for alkali-bearing emeralds (Fig. 9), with types I and II H_2O absorption features, besides features related to the presence of CO_2 molecules (*cf.* Wood and Nassau 1967, 1968, Schmetzer *et al.* 1997, Rondeau *et al.* 2008, Zwaan *et al.* 2012). The features centered at 7,098 and 5,275 cm^{-1} are

Table 2. Laser ablation-inductively coupled plasma-mass spectrometry (LA-ICP-MS) minor and trace element composition of Paraná emerald samples.

Sample	EM21	ML01A	ML01B	ML01C	ML02	ML03	ML04*	ML05*	ML07*	ML08	ML09A	ML09B
Li (ppm)	125.87	195.83	183.74	217.32	160.98	98.79	381.17	171.02	366.58	86.54	325.22	353.15
B	1.61	2.58	1.62	3.24	2.83	4.41	1.95	2.31	2.79	2.90	2.47	1.96
Ge	0.84	0.58	0.55	0.66	0.48	0.59	0.83	0.85	0.77	0.72	0.59	0.71
Rb	32.76	63.22	78.61	68.78	133.00	140.36	64.99	104.02	107.47	142.14	62.48	72.87
Cs	1,331.27	1,553.11	1,875.86	1,619.03	2,035.79	5,110.79	2,959.10	5,595.66	5,452.48	5,970.31	1,708.37	2,466.92
Na	3,900.05	8,393.88	9,146.13	8,631.43	13,807.80	14,480.79	4,015.59	11,346.26	5,510.30	14,717.93	4,814.85	5,095.99
Mg	3,309.87	8,637.71	9,501.11	8,833.70	16,705.98	19,791.55	2,971.31	12,801.91	4,787.15	19,964.64	3,690.90	3,958.18
P	< LOD	< LOD	< LOD	< LOD	< LOD	< LOD	< LOD	< LOD	< LOD	< LOD	< LOD	< LOD
K	250.23	441.88	527.90	470.46	1,415.91	1,811.07	254.03	1,350.40	363.01	1,701.44	209.93	213.00
Ca	23.75	69.84	76.60	75.27	342.88	493.74	23.16	229.71	20.63	570.72	21.88	24.89
Sc	23.53	73.99	71.51	82.22	140.23	85.82	23.96	341.94	66.88	121.91	34.33	35.99
Ti	10.03	3.88	3.08	3.48	3.78	44.31	10.08	58.75	14.60	73.47	5.17	9.49
V	52.23	92.80	110.67	106.15	204.07	174.51	44.82	155.49	73.13	169.06	66.06	59.20
Cr	373.55	567.08	616.88	622.99	574.35	149.72	270.17	649.51	275.79	124.75	399.00	501.77
Mn	11.78	30.59	33.02	34.66	50.34	28.41	54.79	86.79	65.18	33.96	54.81	58.12
Fe	3,790.10	5,909.42	6,230.95	6,629.29	11,123.88	12,953.17	3,973.98	14,608.05	6,102.39	12,891.85	4,404.76	4,701.20
Ga	12.18	10.07	10.52	11.47	10.56	11.39	19.99	14.11	27.55	12.69	23.71	24.47

Average of six analyses per sample at different spots; LOD: limit of detection; *crystal also chemically analyzed by electron probe microanalysis.
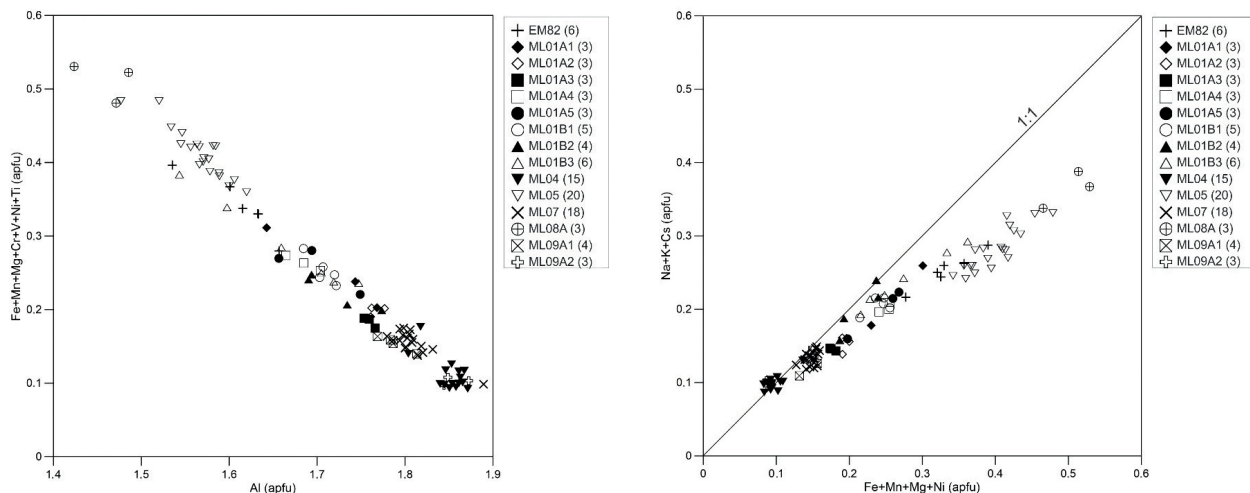

Figure 6. Correlation among different element concentrations for 99 analyzed spots on 15 emerald samples from Paraná. The number of analyzed spots per sample is given in parentheses. (A) Al versus the sum of other Y-site cations. (B) Bivalent Y-site cations versus monovalent channel-site cations. Diagrams after Groat *et al.* (2008).
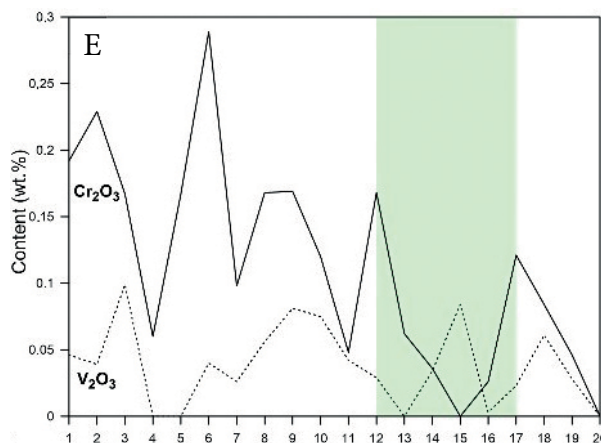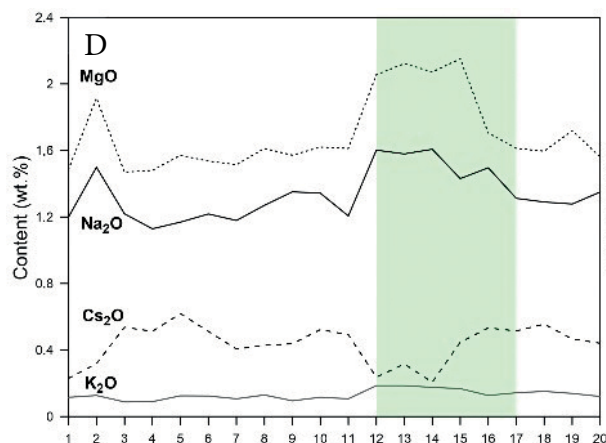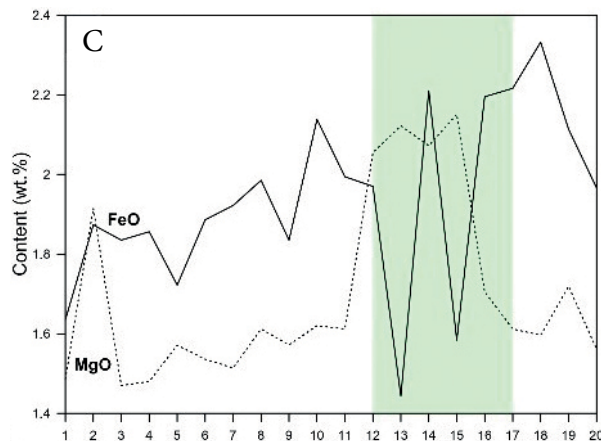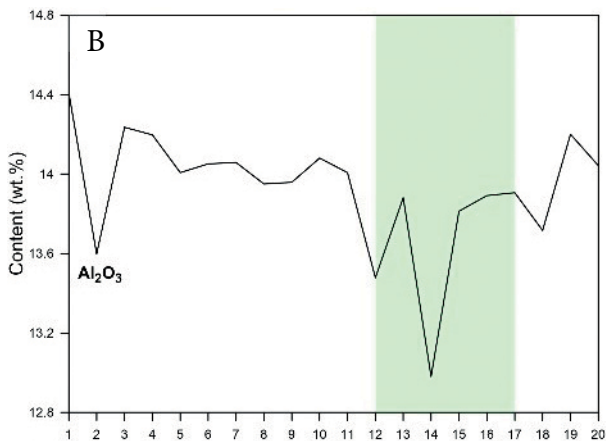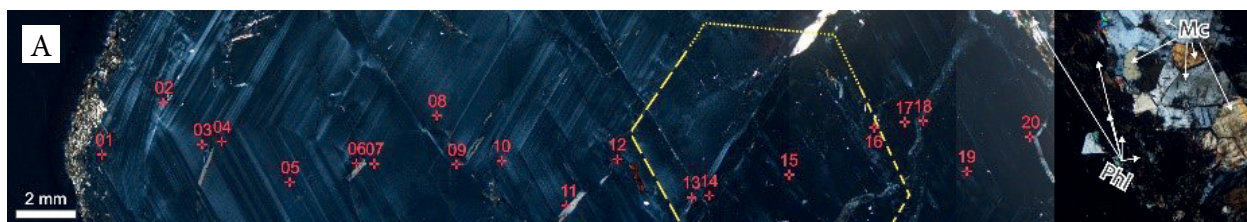
Mc: microcline; Phl: phlogopite.

Figure 7. Electron probe microanalysis analysis along a transversal profile in a color-zoned emerald crystal (sample ML05). (A) Basal section of sample ML05 showing the locations of the analytical EPMA spots. Crossed nicols. The diagrams show concentrations of (B) Al_2O_3, (C) FeO, MgO, (D) Na_2O, Cs_2O, K_2O, (E) Cr_2O_3 and V_2O_3 along the profile. The green columns mark the analyses located in the colorless crystal core.
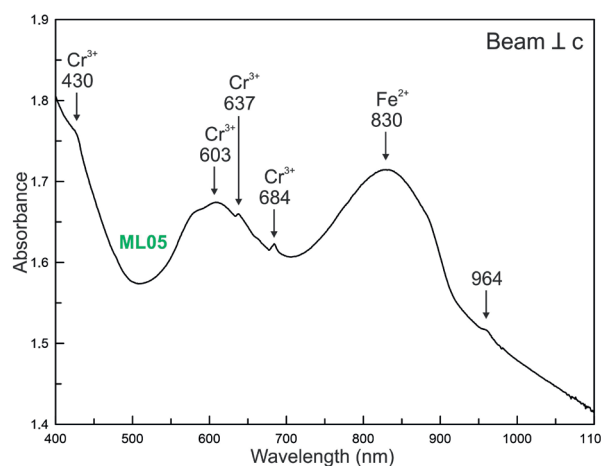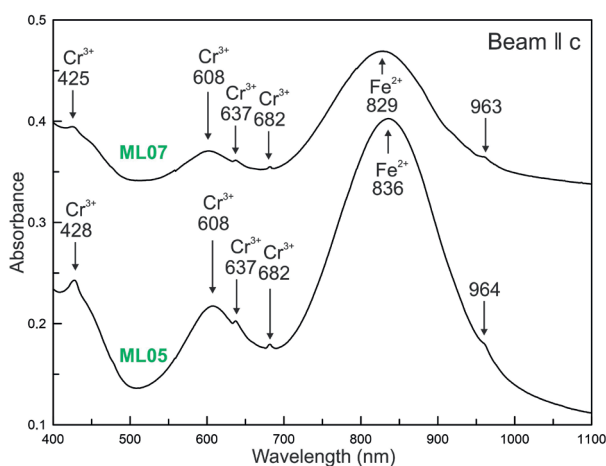
Figure 8. Visible and near infrared absorption spectra of Paraná emeralds. The spectra were obtained with incident beam parallel to the c axis (Beam || c) and perpendicular to the c axis (Beam ⊥ c).
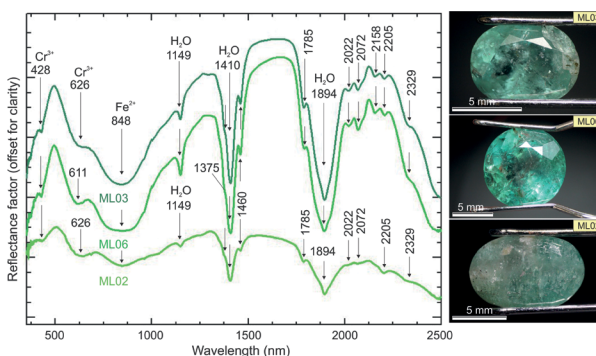
attributed to H_2O II molecules (*i.e.*, water molecules associated with alkali ions in the beryl structural channels; Wood and Nassau 1968). Subtle absorption features at 7,142, 5,448 and 5,100 cm^{-1} are associated with the presence of H_2O I, and a large band between 4,000 and 3,350 cm^{-1} is related to the presence of both types of water molecules. The presence of CO_2 is marked by a sharp absorption feature at 2,359 cm^{-1}. Rondeau *et al.* (2008) also attribute the subtle absorption at the 2,376–2,378 cm^{-1} range to the CO_2 molecule; therefore,
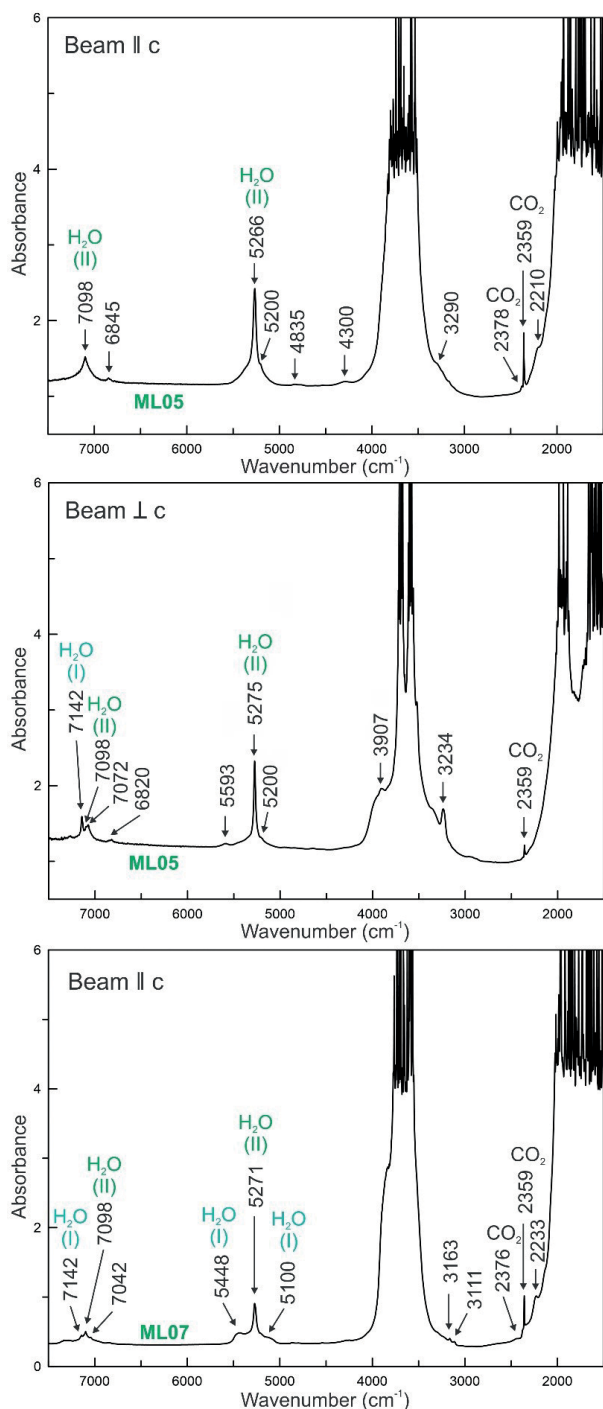
these features may be derived from the isotopic effect of the combination of ^{13}C and [18]O.

Reflectance spectroscopy was applied in three faceted emeralds, since it is a non-destructive method that does not need further sample preparation (Fig. 10). The Paraná emeralds show absorption features in the VNIR range at 428 and 611–629 nm related to electronic transitions in Cr^{3+}, and a broad band centered at 848 nm derived from electronic transitions in Fe^{2+} at the octahedral Y-site (Wood and Nassau 1968, Rondeau *et al.* 2008, Zwaan *et al.* 2012). In the SWIR range, the emeralds show weak absorption features at 1,149 nm, three sharp features between 1,375–1,460 nm (center at 1,410 nm) and other three sharp features between 1,785–2,022 nm (center at 1,894 nm), all attributed to vibrational processes of types I and II water molecules (*cf.* Wood and Nassau 1967, 1968, Clark *et al.* 1990, Schmetzer *et al.* 1997, Rondeau *et al.* 2008). Four other absorption features centered at 2,072, 2,158, 2,205 and 2,329 nm were observed, but not identified.

THERMAL ANALYSIS

Differential thermal and thermal gravimetric analyses performed on three pulverized emerald samples demonstrate an endothermic reaction curve with maximum peak at 921–933°C (Fig. 11). At least two mass loss events by dehydration are registered at the temperatures of 300–500°C and 800–1,050°C. The total water loss varies from 1.85 to 2.13 wt.% at 1,050°C. Sample ML05 registered the higher water loss (2.13%), which concurs with the high H_2O content calculated by the empirical equation of Marshall *et al.* (2016).

The possible dehydration process starts with the loss of H_2O I and/or H_2O IId (doubly coordinated water), and then, at temperatures higher than 800°C, there is the release of H_2O IIs (singly coordinated water). This sequence is a result of the bond strength of each type of water molecule and the balance of forces at the structural channels, based on topology calculation and bond valence (*cf.* Fukuda and Shinoda 2008, Fridrichová *et al.* 2016). Therefore, the mass loss at 300–550°C is attributed to the release of water types IId and/or I. Further mass loss at 800–1,050°C is associated with the loss of water type IIs.

Figure 9. Fourier transform infrared (FTIR) absorption spectra of Paraná emeralds. The spectra were obtained with incident beam parallel to the c axis (Beam || c) and perpendicular to the c axis (Beam ⊥ c).

Figure 10. Staked reflectance spectra of faceted emerald samples. Average of five, four, and three spectral analyses for samples ML03, ML06 and ML02, respectively.

DISCUSSION

Emerald mineralization in the Paraná region is a schist-type deposit controlled by a major shear zone. Chromium and Be sources are probably linked to spatially associated mafic rocks (metamorphosed into amphibolite) and Be-bearing pegmatites, respectively. Although beryl has not been found yet in meter-sized pegmatites lenses associated with the host rocks, emerald crystals can be commonly found in small pegmatite and aplite veins within the schist foliation. In addition, beryl-bearing pegmatites within regional shear zones are reported few kilometers east of the Paraná deposit (Barreto 1991). The presence of Na-rich plagioclase bodies associated with the emerald mineralization suggests metasomatic modification of granitic pegmatites through desilication (Giuliani *et al.* 1990,

Walton 2004). These so-called desilicated pegmatites or albitites are common to several Brazilian metasomatic emerald deposits, such as Carnaíba and Socotó — Bahia state (Giuliani *et al.* 1990) and Fazenda Bonfim — Rio Grande do Norte state (Zwaan *et al.* 2012).

The refractive indices for Paraná crystals are relatively high, but fall within the range expected for most natural emeralds, which is between 1.570 and 1.600 for the ordinary ray, and 1.564–1.593 for the extraordinary ray (Schwarz 1987). It is difficult to establish individual influences of the factors that have an increasing effect on refractive indices, but the presence of structural water and alkaline ions (specially Na and Cs) and the high concentration of Fe and Mg are probably the main characteristics of Paraná emeralds. These high refractive indices, according to Zwaan *et al.* (2012), are common for schist-related emerald deposits.

The absence of reaction through Chelsea filter observation is typical for emeralds with high Fe content (*e.g.,* South Africa and India emeralds; Webster 1975). Two-phase fluid inclusion is the main group of inclusions found in emerald crystals, but mineral inclusions such as mica (possibly phlogopite), feldspar and quartz were also identified. The non-appearance of pyrite inclusions can distinguish Paraná emeralds from Bahia ones, including those from Socotó and Carnaíba (*cf.* Schwarz 1987). Furthermore, the absence of amphibole inclusions is characteristic, since it is a common mineral inclusion in emeralds of other schist-related deposits of Brazil and around the globe (Schwarz 1987, 1998, Zwaan *et al.* 2005, 2012). Additionally, the color zoning accompanied by two-phase fluid inclusions concentration zones suggest an abrupt change in the physicochemical conditions of the environment at crystal growth (Schwarz 1987). Nevertheless, these internal features are very similar to those of Bonfim emeralds (Zwaan *et al.* 2012). Thus, additional chemical characterization should be performed for source mine identification.

According to the Schwarz (1987) empirical subdivision for Cr_2O_3, FeO, MgO and Na_2O concentration ranges in emeralds, the Paraná emerald presents low Cr, medium to high Fe, medium to low Mg and Na. The main trivalent cations replacing Al^{3+} at the octahedral Y-site are Cr^{3+}, V^{3+} and possibly Fe^{3+}. Heterovalent substitution plays a major role at the octahedral Y-site, with the entry of Fe^{2+} and Mg^{2+} coupled with Na^+ and other monovalent cations entrance at the channel sites. Figure 12A shows the relative concentration of the main substituents of octahedral Al for Paraná emerald and other deposits around the world. Magnesium is the main substituent for most of the samples, but Paraná emerald also contains Fe in similar proportions. In Figure 12B, the relative concentration of chromophore elements for Paraná emerald evidences that it is one of the highest Fe-rich emeralds among several other deposits. The comparison with other Brazilian emeralds is presented in Figures 13A and 13B, and the high Fe content allows the individualization of Paraná deposit from the others.

Zwaan *et al.* (2012) proposed several diagrams for discriminating Fazenda Bonfim deposit and other different schist-related emerald deposits, by plotting LA-ICP-MS chemical data. The Fazenda Bonfim deposit presents strong geological similarities with the
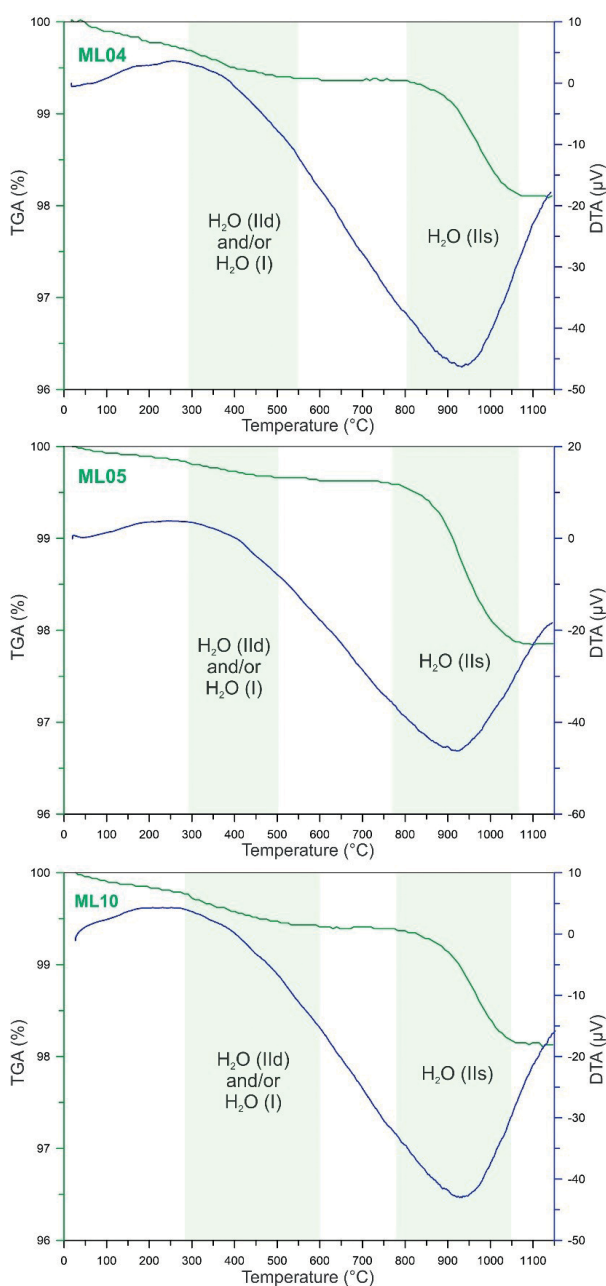

Figure 11. Thermogravimetric analysis/differential thermal analysis (TGA/DTA) curves of pulverized emerald samples. The green rectangles delimit the zones of the corresponding water molecule loss from the channel-sites.

Paraná deposit, including association with phlogopite schists and granitic intrusions, as well as being affected by transcurrent shear zones within the Rio Grande do Norte Sub-province (Zwaan *et al.* 2012, Santiago *et al.* 2018). In the K-(Li+Cs)-Rb ternary diagram, Paraná emeralds can be individualized by their higher amount of Li+Cs, especially for their high Cs content (Fig. 14).

Despite the low content of Cr^{3+}, both absorption and reflectance spectra of the Paraná emeralds are typical of Cr-emeralds (Schmetzer *et al.* 1974, Zwaan 2006). They have absorption features at 428, 608, 637, and 683 nm associated with the presence of Cr^{3+}. Therefore, the absorption features derived from electronic transitions in Cr^{3+} and the weak absorption in the green range are responsible for its green coloration. This statement is in consonance with the decrease of Cr_2O_3 at the colorless core zones in zoned crystals (Fig. 7E). The presence of Fe^{2+} broad absorption feature at ~830 nm does not influence its coloration, since it is situated outside the visible range (*cf.* Zwaan 2006). The spectra obtained for the ML05 sample cut
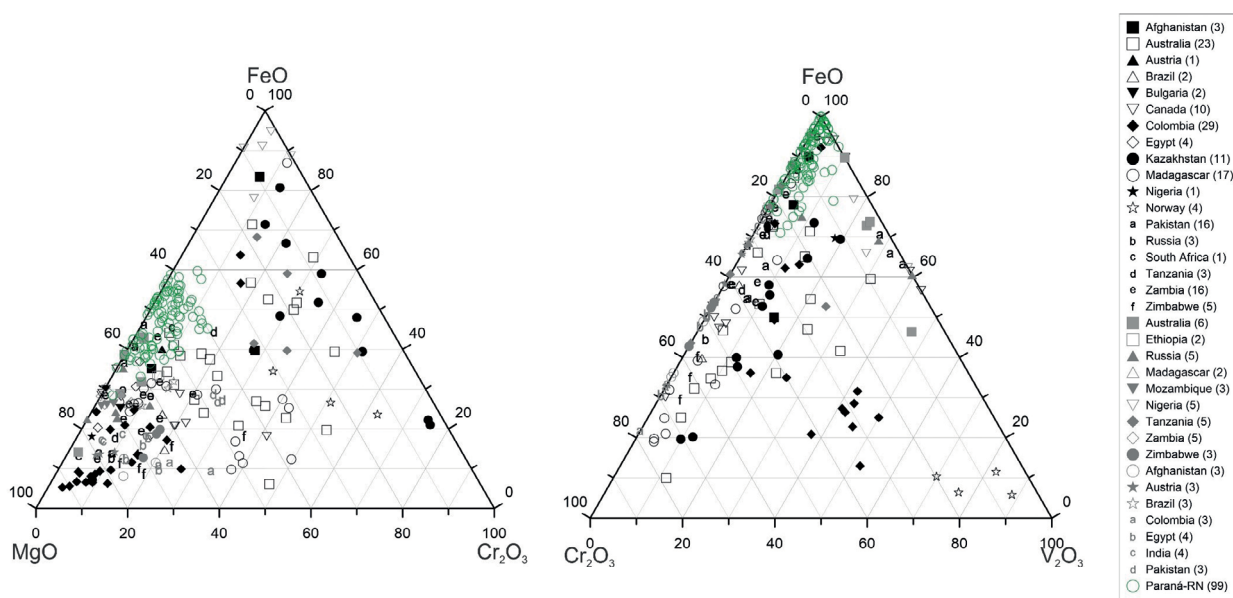
Figure 12. Ternary composition diagrams for Paraná emeralds and worldwide deposits. (A) Composition in terms of main Y-site Al-substituents (MgO-FeO-Cr_2O_3). (B) Composition in terms of main chromophore elements in emerald (FeO-Cr_2O_3-V_2O_3). Results shown for 210 analyses from literature and 99 analyses of Paraná emerald. The number of analyses per country is given in parenthesis. Symbols in black were compiled from Groat *et al.* (2008), which has as source of data: Kovaloff (1928), Zambonini and Caglioto (1928), Leitmeier (1937), Otero Muñoz and Barriga Villalba (1948), Simpson (1948), Gübelin (1958), Vlasov and Kutakova (1960), Martin (1962), Petrusenko *et al.* (1966), Beus and Mineev (1972), Garstone (1981), Hanni and Klein (1982), Graziani *et al.* (1983), Kozlowski *et al.* (1988), Hammarstrom (1989), Ottaway (1991), Schwarz (1991), Abdallah and Mohamed (1999), Gavrilenko and Pérez (1999), Alexandrov *et al.* (2001), Groat *et al.* (2002), Marshall *et al.* (2004), Vapnik *et al.* (2005, 2006), Zwaan *et al.* (2005), Gavrilenko *et al.* (2006) and Zwaan (2006). Symbols in grey were compiled from Aurisicchio *et al.* (2018). The diagrams are after Hammarstrom (1989).
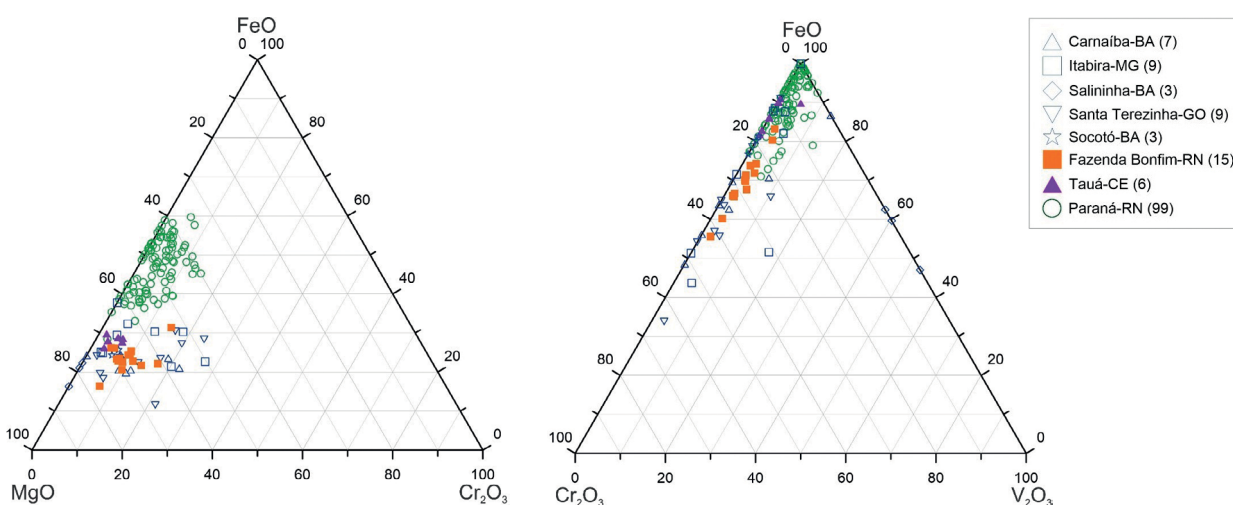
Figure 13. Ternary composition diagrams for Brazilian emeralds. (A) Composition in terms of main Y-site Al-substituents (MgO-FeO-Cr_2O_3). (B) Composition in terms of the main chromophore elements in emerald (FeO-Cr_2O_3-V_2O_3). Results shown for 52 analyses from literature and 99 of the Paraná emerald. The number of analyses per deposit is given in parenthesis. Fazenda Bonfim data compiled from Zwaan *et al.* (2012). Other chemical data compiled from Schwarz (1987), which has as source of data: Graziani and Lucchesi (1979), Hanni (1982), Hanni and Kerez (1983), Eidt and Schwarz (1987), Hanni et al. (1987) and Schwarz (1987). The diagrams are after Hammarstrom (1989).

in different positions (parallel and perpendicular to the c axis) show variations in the maximum absorption centralization, as well as a variation of the relative absorbance values, which reflects the strong dichroism of Paraná emeralds (Fig. 3C).

FTIR spectra are consistent with alkali-rich emeralds (*cf.* Zwaan *et al.* 2012), with absorption features related to the presence of types I and II water (Fig. 8). The high content of sodium and the large water loss associated with type II water molecule suggest that the presence of type II H_2O in the structural channels is more expressive than type I H_2O. Additionally, some CO_2 molecules can also be expected, as evidenced by an absorption feature at 2,359 cm^{-1}.

CONCLUSIONS

The Paraná emerald deposit, located at Rio Grande do Norte Sub-province of the Borborema Province, NE Brazil, is characterized by emerald-bearing granitic aplite and pegmatite veins within phlogopite and actinolite phlogopite schists associated with granite pegmatite bodies and desilicated pegmatites (albitites). These rocks form a mylonitic melange along the Portalegre Shear Zone. Interaction between such rocks at high temperature shearing most certainly allowed the mobilization of Be and chromophore elements, such as Cr, Fe and V to form emerald.

Our study has shown that Paraná emeralds have a main bluish green color, although they are typically dichroic, varying from greenish blue to yellowish green. These crystals are colored mostly by Cr, as evidenced by its characteristic absorption spectra and color zoning chemistry. However, due to its elevated Fe content, they exhibit broad absorption features at ~830 nm and do not show reaction through Chelsea filter, which can be a diagnostic criterion to distinguish Paraná emeralds from several other schist-related deposits. Additionally, the high refractive indices, the presence of numerous two-phase fluid inclusions and partially healed fissures, and the absence of pyrite and amphibole as mineral inclusions can also be used as criteria for distinction from other Brazilian emeralds, such as those from Santa Terezinha (GO), Carnaíba (BA), Socotó (BA), Itabira (MG), and Tauá (CE).

When comparing our results with available data from Fazenda Bonfim emerald deposit, also located in Rio Grande do Norte Sub-province, there is some overlap when it comes to geological setting and internal features, but one can be easily differentiated from the other by its chemical composition. The Paraná emeralds show higher FeO content and lower Cr_2O_3. The alkali concentration can also be used for discriminating purposes, especially due to the elevated Cs content in Paraná emeralds, although spectroscopically they both show characteristics for alkali emeralds with strong absorption features related to the presence of type II water.

Future research at the Paraná deposit could focus on structural analysis, whole-rock/mineral geochemistry and isotope geology aiming to define mineralization controls and evolution, contributing to better understand the Borborema Province metallogenetic scenario.
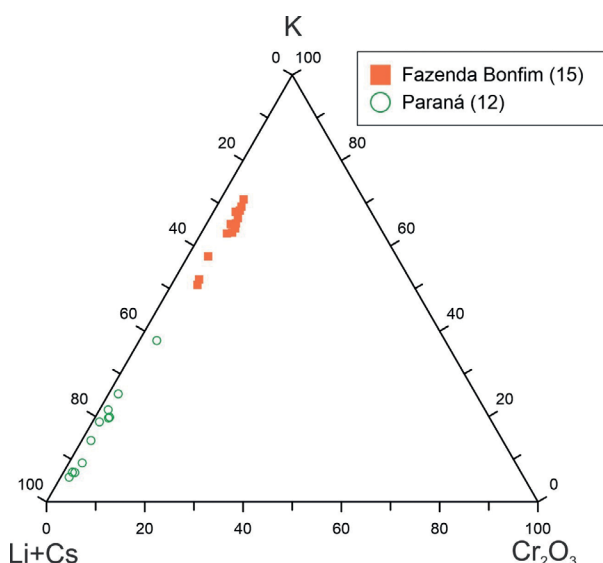
Figure 14. Ternary K-(Li+Cs)-Rb diagram for emeralds from Rio Grande do Norte sub-province. Average values in ppm obtained by laser ablation-inductively coupled plasma-mass spectrometry (LA-ICP-MS) for 12 samples from Paraná and 15 from Fazenda Bonfim. Data from Fazenda Bonfim compiled from Zwaan *et al.* (2012). Diagram after Zwaan *et al.* (2012).

REFERENCES

Abdalla H.M., Mohamed F.H. 1999. Mineralogical and geochemical investigation of emerald and beryl mineralisation, Pan-African Belt of Egypt: genetic and exploration aspects. *Journal of African Earth Sciences*, **28**(3):581-598. https://doi.org/10.1016/S0899-5362(99)00033-0

Alexandrov P., Giuliani G., Zimmermann J.L. 2001. Mineralogy, age and fluid geochemistry of the Rila Emerald deposits, Bulgaria. *Economic Geology*, **96**(6):1469-1476. https://doi.org/10.2113/gsecongeo.96.6.1469

Araújo Neto J.F., Lira Santos G., Souza I.M.B.A., Barreto S.B., Santos L.C.M.L., Bezerra J.P.S., Carrino T.A. 2018. Integration of remote sensing, airborne geophysics and structural analysis to geological mapping: a case study of the Vieirópolis region, Borborema Province, NE Brazil. *Geologia USP. Série Científica*, **18**(3):89-103. https://doi.org/10.11606/issn.2316-9095.v18-140834

Aurisicchio C., Conte A.M., Medeghini L., Ottolini L., De Vito C. 2018. Major and trace element geochemistry of emerald from several deposits: Implications for genetic models and classification schemes. *Ore Geology Reviews*, **94**:351-366. http://dx.doi.org/10.1016/j.oregeorev.2018.02.001

Barreto S.B. 1991. *Caracterização químico-mineralógica dos berilos de Tenente Ananias – RN*. MS Dissertation, Instituto de Geociências, Universidade Federal de Pernambuco, Recife, 219 p.

Beus A.A., Mineev D.A. 1972. *Some Geological and Geochemical Features of the Muzo-Coscuez Emerald Zone, Cordillera Oriental, Colombia*. Empresa Colombiana de Minas, 55 p.

Bragg W.L., West J. 1926. The structure of beryl, $Be_3Al_2Si_6O_{18}$. *Proceedings of the Royal Society of London*, **111**:691-714.

Brito Neves B.B., Santos E.J., Van Schmus W.R. 2000. Tectonic History of the Borborema Province. In: Cordani U.G., Milani E.J., Tomaz Filho A., Campos D.A. (eds.), Tectonic Evolution of South America. *31st International Geological Congress*. Rio de Janeiro, p. 151-182.

Cavalcanti Neto M.T.O., Barbosa R.V.N. 2007. As esmeraldas de Lajes, Caiçara do Rio dos Ventos e São Tomé/RN. *Holos*, **2**:92-104. https://doi.org/10.15628/holos.2007.103

Clark R.N., King T.V.V., Klejwa M., Swayze G.A., Vergo N. 1990. High spectral resolution reflectance spectroscopy of minerals. *Journal of Geophysical Research*, **95**(B8):12653-12680. https://doi.org/10.1029/JB095iB08p12653

Eidt T., Schwarz D. 1987. Die Smaragde von Carnaíba, Bahia, Brasilien; Vorkommen und Charakteristika. *Zeitschrift der Deutsche Gemmologische Gesellschaft*, **36**:3-4.

Fridrichová J., Bacik P., Bizovská V., Libowitzky E., Škoda R., Uher P., Ozdín D., Števko M. 2016. Spectroscopic and bond-topological investigation of interstitial volatiles in beryl from Slovakia. *Physics and Chemistry of Minerals*, **43**(6):419-437. https://doi.org/10.1007/s00269-016-0806-9

Fukuda J., Shinoda K. 2008. Coordination of water molecules with Na^+ cations in a beryl channel as determined by polarized IR spectroscopy. *Physics and Chemistry of Minerals*, **35**(6):347-357. http://dx.doi.org/10.1007/s00269-008-0228-4

Garstone J.D. 1981. The geological setting and origin of emeralds from Menzies, Western Australia. *Journal of the Royal Society of Western Australia*, **64**:53-64.

Gavrilenko E.V., Pérez B.C. 1999. Characterisation of emeralds from the Delbegetey deposit, Kazakhstan. In: Stanley C.J. *et al.* (eds.), *Mineral Deposits:* Processes to Processing. Rotterdam: Balkema, p. 1097-1100.

Gavrilenko E.V., Pérez B.C., Bolibar R., Garcia Del Amo D. 2006. Emeralds from the Delbegetey deposit (Kazakhstan): mineralogical characteristics and fluid inclusion study. *Mineralogical Magazine*, **70**(2):159-173. https://doi.org/10.1180/0026461067020321

Giuliani G., Silva L.J.H.D., Couto P. 1990. Origin of emerald deposits of Brazil. *Mineralium Deposita*, **25**(1):57-64. https://doi.org/10.1007/BF03326384

Graziani G., Gübelin E., Lucchesi S. 1983. The genesis of an emerald from the Kitwe District, Zambia. *Neues Jahrbuch für Mineralogie Monatshefte*, **4**:75-186.

Graziani G., Lucchesi S. 1979. Einschlusse und Genese eines Vanadiumberylis von Salininha/BA, Brasilien. *Zeitschrift der Deutsche Gemmologische Gesellschaft*, **28**(3):134-145.

Groat L.A., Giuliani G., Marshall D.D., Turner D. 2008. Emerald deposits and occurrences: A review. *Ore Geology Reviews*, **34**:87-112.

Groat L.A., Marshall D.D., Giuliani G., Murphy D.C., Piercey S.J., Jambor J.L., Mortensen J.K., Ercit T.S., Gault R.A., Mattey D.P., Schwarz D., Maluski H., Wise M.A., Wengzynowski W., Eaton D.W. 2002. Mineralogical and geochemical study of the Regal Ridge Emerald Showing, Southeastern Ukon. *The Canadian Mineralogist*, **40**(5):1313-1338.

Gübelin E.J. 1958. Emeralds from Sandawana. *Journal of Gemmology*, **6**(8):340-354.

Hammarstrom J.M. 1989. Mineral chemistry of emeralds and some minerals from Pakistan and Afghanistan: an electron microprobe study. In: Kazmi A.H., Snee I.W. (eds.), *Emeralds of Pakistan:* Geology, Gemology and Genesis. New York: Van Nostrand Reinhold, p. 125-150.

Hanni H.A. 1982. A contribution to the separability of natural and synthetic emeralds. *Journal of Gemmology*, **18**(2):138-143.

Hanni H.A., Kerez C.J. 1983. Neues vom Smaragd-Vorkommen von Sta. Terezinha de Goiás, Brasilien. *Zeitschrift der Deutschen Gemmologischen Gesellschaft*, **32**(1):50-58.

Hanni H.A., Klein H.H. 1982. Ein Smaragdvorkommen in Madagaskar. *Zeitschrift der Deutschen Gemmologischen Gesellschaft*, **21**:71-77.

Hanni H.A., Schwarz D., Fishcer M. 1987. Die Smaragde der Belmont Mine bei Itabira, Minas Gerais, Brasilien; Vorkommen und Charakteristika. *Zeitschrift der Deutschen Gemmologischen Gesellschaft*, **36**(1-2):33-49.

Jochum K.P., Weis U., Stoll B., Kuzmin D., Yang Q., Raczek I., Jacob D.E., Stracke A., Birbaum K., Frick D.A., Günther D., Enzweiler J. 2011. Determination of reference values for NIST SRM 610-617 glasses following ISO guidelines. *Geostandards and Geoanalytical Research*, **35**(4):397-429. https://doi.org/10.1111/j.1751-908X.2011.00120.x

Kovaloff P. 1928. Geologist's report on Somerset emeralds. *South African Mining and Engineering Journal*, **39**:101-103.

Kozlowski A., Metz P., Estrada Jaramillo H.A. 1988. Emeralds from Somondoco, Colombia: chemical composition, fluid inclusions and origin. *Neues Jahrbuch für Mineralogie – Abhandlungen*, **159**(1):23-49.

Leitmeier H. 1937. Das Smaragdvorkommen in Habachtal in Salzburg und seine Mineralien. *Tschermak's Mineralogische und Petrographische Mitteilungen*, **49**:245-368.

Malvern Panalytical. 2018. *ASD FieldSpec 4 Standard-Res Spectroradiometer*. Available at: <https://www.asdi.com/products-and-services/fieldspec-spectroradiometers/fieldspec-4-standard-res/>. Accessed on: Jan. 29, 2019.

Marshall D.D., Downes P.J., Ellis S., Greene R., Loughrey L., Jones P. 2016. Pressure-temperature-fluid constraints for the Poona emerald deposits, Western Australia: fluid Inclusion and stable isotope studies. *Minerals*, **6**(4):130-152. https://doi.org/10.3390/min6040130

Marshall D.D., Groat L.A., Falck H., Giuliani G., Neufeld H.L.D. 2004. The Lened emerald prospect, Northwest Territories, Canada: insights from fluid inclusions and stable isotopes, with implications for northern Cordilleran emerald. *Canadian Mineralogist*, **42**(5):1523-1539. https://doi.org/10.2113/gscanmin.42.5.1523

Martin H.J. 1962. Some observations on southern Rhodesian emeralds and chrysoberyls. *Journal of the Chamber of Mines*, **4**(10):34-38.

Medeiros V.C. (ed.). 2008. *Geologia e Recursos Minerais da Folha Sousa SB.24-Z-A*. Escala 1:250.000. Recife: CPRM – Serviço Geológico do Brasil, 312 p.

Moraes J.F.S. 1999. *Gemas do Estado do Rio Grande do Norte*. Recife: CPRM – Serviço Geológico do Brasil, 72 p.

Otero Muñoz G., Barriga Villalba A.M. 1948. *Esmeraldas de Colombia*. Bogota: Banco de la Republica, 133 p.

Ottaway T.L. 1991. *The Geochemistry of the Muzo Emerald Deposit, Colombia*. MS Dissertation, University of Toronto, Toronto, 216 p.

Petrusenko S., Arnaudov V., Kostov I. 1966. Emerald pegmatite from the Urdini Lakes, Rila Mountains. *Annuaire de l'Université de Sofia,* **59**:247-268.

Rondeau B., Fritsch E., Peucat J., Nordrum F.S., Groat L. 2008. Characterization of Emeralds from a historical deposit: Byrud (Eidsvoll), Norway. *Gems and Gemology*, **44**(2):108-122. https://doi.org/10.5741/GEMS.44.2.108

Santiago J.S., Souza V.S., Filgueiras B.C., Jiménez F.A.C. 2018. Emerald from the Fazenda Bonfim Deposit, northeastern Brazil: chemical, fluid inclusions and oxygen isotope data. *Brazilian Journal of Geology*, **48**(3):457-472.

Santos E.J., Souza Neto J.A., Silva M.R.R., Beurlen H., Cavalcanti J.A.D., Silva M.G., Dias V.M., Costa A.F., Santos L.C.M.L., Santos R.B. 2014. Metalogênese das porções norte e central da Província Borborema. In: Silva M.G., Rocha Neto M.B., Jost H., Kuyumijan R.M. (eds.), *Metalogênese das províncias tectônicas brasileiras*. Belo Horizonte: CPRM, p. 343-388.

Schmetzer K., Berdesinski W., Bank H. 1974. Über die Mineralart Beryll, ihre Farben und Absorptionsspektren. Zeitschr. *Gemmologischen Gesellschaft*, **23**(1):5-39.

Schmetzer K., Kiefert L., Bernhardt H., Beili Z. 1997. Characterization of Chinese hydrotermal synthetic emerald. *Gems and Gemology*, **33**(4):276-291. https://doi.org/10.5741/GEMS.33.4.276

Scholz R., Romano A.W., Belotti F.M., Chaves M.L.S.C. 2010. Geochemical prospecting of beryl emerald variety in the Fazenda Bonfim region (Lajes, RN). *Geociências*, **29**(4):613-621.

Schwarz D. 1987. *Esmeraldas: inclusões em gemas*. Ouro Preto: Universidade Federal de Ouro Preto (UFOP), Imprensa Universitária, 439 p.

Schwarz D. 1991. Australian emeralds. *Australian Gemmologist*, **17**(12):488-497.

Schwarz D. 1998. The importance of solid and fluid inclusions for the characterization of natural and synthetic emeralds. In: Giard D. (ed.), *L'émeraude*. France: Association Française de Gemmologie, p. 71-80.

Simpson E.S. 1948. Minerals of Western Australia. *Perth Government Printer*, **1**:195-207.

Souza L.C. (ed.). 2017. *Geologia e Recursos Minerais da Folha Pau dos Ferros SB.24-Z-A-II*. Escala 1:100.000. Recife: CPRM - Serviço Geológico do Brasil / Universidade Federal do Rio Grande do Norte, 109 p.

Vapnik Y., Moroz I., Roth M., Eliezri I. 2006. Formation of emeralds at pegmatite-ultramafic contacts based on fluid inclusions in Kianjavato emerald, Mananjary deposits, Madagascar. *Mineralogical Magazine*, **70**(2):141-158. https://doi.org/10.1180/0026461067020320

Vapnik Y., Sabot B., Moroz I. 2005. Fluid inclusions in Ianapera emerald, Southern Madagascar. *International Geology Reviews*, **47**(6):647-662. https://doi.org/10.2747/0020-6814.47.6.647

Vasconcelos F.J.C. 1984. *Ocorrência de esmeralda em Pitombeiras, município de Paraná, Estado do Rio Grande do Norte*. Especialização em Gemologia, Instituto de Geociências, Universidade Federal de Minas Gerais, Belo Horizonte, 36 p.

Viegas L.G.F., Archanjo C.J., Hollanda M.H.B.M., Vauchez A. 2014. Microfabrics and zircon U-Pb (SHRIMP) chronology of mylonites from the Patos shear zone (Borborema Province, NE Brazil). *Precambrian Research*, **243**:1-17. http://dx.doi.org/10.1016/j.precamres.2013.12.020

Vlasov K.A., Kutakova E.I. 1960. *Izumrudnye Kopi*. Moscow: Moscow Akademia Nauk SSGR, 252 p.

Walton L. 2004. *Exploration criteria for coloured gemstone deposits in the Yukon*. Yukon: Yukon Geological Survey, 184 p.

Webster R. 1975. *Gems, their sources, descriptions and identification*. 3ª ed. London: Butterworth and Co. Publishers, 938 p.

Wood D.L., Nassau K. 1967. Infrared spectra of foreign molecules in beryl. *Journal of Chemical Physics*, **47**:2220-2228. https://doi.org/10.1063/1.1703295

Wood D.L., Nassau K. 1968. The characterization of beryl and emerald by visible and infrared absorption spectroscopy. *The American Mineralogist*, **53**(5-6):777-800.

Zambonini F., Caglioto V. 1928. Ricerche chimiche sulla rosterite di San Piero in Campo (Isola d'Elba) e sui berilli in generale. *Gazzetta Chimica Italiana*, **58**:131-152.

Zwaan J.C. 2006. Gemmology, geology and origin of the Sandawana emerald deposits, Zimbabwe. *Scripta Geologica*, **131**:1-211.

Zwaan J.C., Jacob D.E., Haeger T., Cavalcanti Neto M.T.O., Kanis J. 2012. Emeralds from the Fazenda Bonfim Region, Rio Grande do Norte, Brazil. *Gems and Gemology*, **48**(1):2-17. http://dx.doi.org/10.5741/GEMS.48.1.2

Zwaan J.C., Seifert A., Vrána S., Laurs B.M., Anckar B., Simmons W.B., Falster A.U., Lustenhouwer W.J., Koivula J.I., Garcia-Guillerminet H. 2005. Emeralds from the Kafubu area, Zambia. *Gems and Gemology*, **41**(2):2-34. https://doi.org/10.5741/GEMS.41.2.116